Geophysical Journal International

Geophys. J. Int. (2012) **188,** 1103–1116 doi: 10.1111/j.1365-246X.2011.05296.x

Sensitivity of broad-band ground-motion simulations to earthquake source and Earth structure variations: an application to the Messina Straits (Italy)

W. Imperatori[1] and P. M. Mai[2]

[1]*Institute of Geophysics, ETH Zurich, Sonneggstr. 5,* CH-8092 *Zurich, Switzerland. E-mail: imperatori@tomo.ig.erdw.ethz.ch*
[2]*Division of Physical Sciences and Engineering, KAUST, Thuwal* 23955-6900*, Saudi Arabia*

Accepted 2011 November 9. Received 2011 August 30; in original form 2011 July 13

SUMMARY

In this paper, we investigate ground-motion variability due to different faulting approximations and crustal-model parametrizations in the Messina Straits area (Southern Italy). Considering three 1-D velocity models proposed for this region and a total of 72 different source realizations, we compute broad-band (0–10 Hz) synthetics for M_w 7.0 events using a fault plane geometry recently proposed.

We explore source complexity in terms of classic kinematic (constant rise-time and rupture speed) and pseudo-dynamic models (variable rise-time and rupture speed). Heterogeneous slip distributions are generated using a Von Karman autocorrelation function. Rise-time variability is related to slip, whereas rupture speed variations are connected to static stress drop. Boxcar, triangle and modified Yoffe are the adopted source time functions.

We find that ground-motion variability associated to differences in crustal models is constant and becomes important at intermediate and long periods. On the other hand, source-induced ground-motion variability is negligible at long periods and strong at intermediate-short periods. Using our source-modelling approach and the three different 1-D structural models, we investigate shaking levels for the 1908 M_w 7.1 Messina earthquake adopting a recently proposed model for fault geometry and final slip. Our simulations suggest that peak levels in Messina and Reggio Calabria must have reached 0.6–0.7 g during this earthquake.

Key words: Seismology; Earthquake ground motion; Computational seismology.

1 INTRODUCTION

Over the last three decades, seismologists have introduced several analytical and numerical techniques to compute synthetics seismograms. Despite the increase in complexity, their applicability to high-frequency ground-motion prediction for engineering purposes is hampered by the still limited knowledge of small-scale crust heterogeneities and fine rupture process details.

To partially overcome these limitations, researchers have proposed different approaches, the most important being empirical Green's functions (Irikura 1986; Kamae *et al.* 1998) and purely stochastic (Boore 1983) ones. However, in recent years the attention has been focused on the simulation of realistic broad-band (0–10 Hz) ground-motion synthetics through so-called hybrid techniques (e.g. Pitarka *et al.* 2000; Liu *et al.* 2006; Mai *et al.* 2010). Their main advantage compared to the other methods is that the computed wavefield still presents a deterministic component at low frequency, thus reflecting the effects of rupture processes and large-scale crust heterogeneities. Scattering effects become dominant only at higher frequencies.

Such broad-band simulation approaches are increasingly applied to reliably estimate possible ground shaking levels for future events (Graves *et al.* 2008). Compared to estimating the shaking levels in potential future earthquake based on empirical ground motions prediction equations, simulation-based methods offer several advantages, the most important being the explicit consideration of the effects of earthquake source, wave-propagation path, and local site effects on ground motions. Moreover, earthquake scenario simulations that generate complete three component broadband synthetics represent an important resource for earthquake engineering and structural design. At the same time the simulation approach can be applied to past events for investigating source and site effects or have a more complete description of the experienced shaking levels, as for example, for the 1906 San Francisco (Aagaard *et al.* 2008), the 1994 Northridge (Hartzell *et al.* 2005) and the 1997 Umbria–Marche (Castro *et al.* 2001) earthquakes.

Generally, studies on earthquake rupture scenario include different realizations of slip, rise-time, rupture-speed, hypocentre and even fault plane positions (or a combination of them) to capture as

much as possible the variability of ground shaking levels. In most cases, these models are purely kinematic but allow for rise-time and rupture speed variations to reproduce the essential features of dynamic faulting process (Guatteri *et al.* 2004; Liu *et al.* 2006; Graves *et al.* 2008). Such variations, although not directly derived from the constitutive relations, are constrained to be consistent with main findings of dynamic rupture studies (e.g. Day 1982; Oglesby & Day 2002; Guatteri *et al.* 2003).

Besides these source-related aspects, complex Earth models can significantly influence the propagating wavefield and hence amplitude, duration and frequency content of ground motions. Considering Green's function variability can be an important issue especially in regions where the Earth structure is particularly complex and no reliable 3-D models are available (e.g. Imperatori *et al.* 2010). Unfortunately, detailed 3-D crustal models are limited to few and small areas worldwide, and usually suffer from limited spatial resolution. In most cases, Earth structure is approximated by one or more 1-D models, generally obtained with different methodologies and data sets. Although in earthquake scenario studies, it is common practice to assume a single velocity model (thought to be the best representative model) and to focus on earthquake source-related effects (Cultrera *et al.* 2010), this study investigates broad-band ground-motion variability by accounting for various 1-D velocity models in the same area. This permits us to explicitly include medium uncertainties on ground shaking estimations and to compare medium influences with respect to those attributed to source terms.

In our study, we consider an area characterized by the highest seismic risk in the Mediterranean region: the Messina Straits (Italy). This region is characterized by significant structural complexities as supported by numerous geological and geophysical studies (Monaco & Tortorici 2000; Barberi *et al.* 2004, among the others), and several 1-D velocity models have been proposed in the recent past by different authors (Barberi *et al.* 2004; Langer *et al.* 2007). Besides exploring ground-motion variability for possible future M_w 7.0 events, we also consider the last strong earthquake that struck the Straits area on 1908 December 28. This highly damaging event was one of the most powerful European earthquakes (M_w 7.1 as estimated by Pino *et al.* 2000) causing tsunami waves and thousands of casualties in the nearby cities (Teramo *et al.* 2008). Many authors have investigated the fault responsible for this earthquake and, due to scarceness of data and their low quality, very different models have been proposed (see Amoruso *et al.* 2002, for a review). Even if the debate is far from being closed, recent models of Pino *et al.* (2000) and Amoruso *et al.* (2006) are currently considered the most reliable ones, though still showing some remarkable differences. Here, we consider a slightly modified version of the original Amoruso *et al.* (2006) model (hereafter referred to as modified Amoruso model) that has been obtained by including all available seismological and geodetic data in a non-linear joint inversion for fault position and slip distribution. In the following, we describe in details the source and the velocity models used in our simulations. Numerical techniques adopted to compute broad-band synthetic seismograms are reported separately. Results are then analysed in context of the different effects on ground motion due to the source terms and structures models. In the last section, we present simulated scenarios for possible future M_w 7.0 events and the historical 1908 Messina Straits event, focusing on the two major cities of Messina and Reggio Calabria.

2 SOURCE MODELS

To study ground-motion variation in terms of scenario calculations for future strong earthquakes in the Messina Straits area, considering both earthquake source and Earth structure effects, we propose four random slip models generated using the procedure described in Mai & Beroza (2002). We fix our target moment magnitude to 7.0 and adopt a fault plane whose orientation and mechanism (Table 1) are equal to those proposed by Amoruso *et al.* (2006). Its position is shown in Fig. 1 along with the irregular receiver grid and the fault plane projection. It is worth noticing that our fault plane (as the modified Amoruso model) differs from that proposed in the Italian database of individual seismogenic sources (Basili *et al.* 2008) in terms of orientation, position and, secondarily, mechanism. Our decision of assuming the Amoruso model geometry as a reference is determined by the fact that it was obtained using all available geophysical data. Note that Zonno *et al.* (2008) deployed the Basili *et al.* (2008) geometry for scenario simulations in the Straits area, applying strongly simplified rupture characterizations and performing high-frequency simulations only. Our broad-band simulations with more physics-based rupture models, resolved onto the Amoruso *et al.* (2006) geometry, thus provides an alternative approach to perform simulation-based shaking scenarios for this region.

The dimensions of the assumed rupture plane are consistent with Wells & Coppersmith (1994) equations for dip-slip events of same magnitude. Rupture models are shown in Fig. 2, and can be classified as single slip-patch and double slip-patch source models. The slip distributions in each class are rather similar to highlight the influence of Earth structure models on the computed ground-motions.

For simulating the 1908 Messina Straits earthquake, we modify the original source model of Amoruso *et al.* (2006) because of its excessive length and keep only the section releasing the largest amount of energy. Discarded areas are characterized by small slip

Table 1. Fault plane and rupture models parameters for the M_w 7.0 scenarios; numbers from 1 to 6 in the rightmost column are used in Figs 7(a) and (b), and indicate the corresponding rupture model. See text for details.

Fault	Slip class	Source-time function	Rupture Model	
Strike : −5.5 °			Variable rise-time – variable rupture speed (supershear)	6
Dip: 42.2 °		Boxcar		
Rake: 242 °	Single patch		Variable rise-time – variable rupture speed (subshear)	5
Width : 20 km			Variable rise-time – constant rupture speed	4
Length: 40 km		Triangle		
			Constant rise-time – variable rupture speed (super-shear)	3
Plane top: 1 km				
Plane bottom: 14.5 km	Double patch	Yoffe	Constant rise-time – variable rupture speed (subshear)	2
Moment magnitude: 7.0			Constant rise-time – constant rupture speed	1

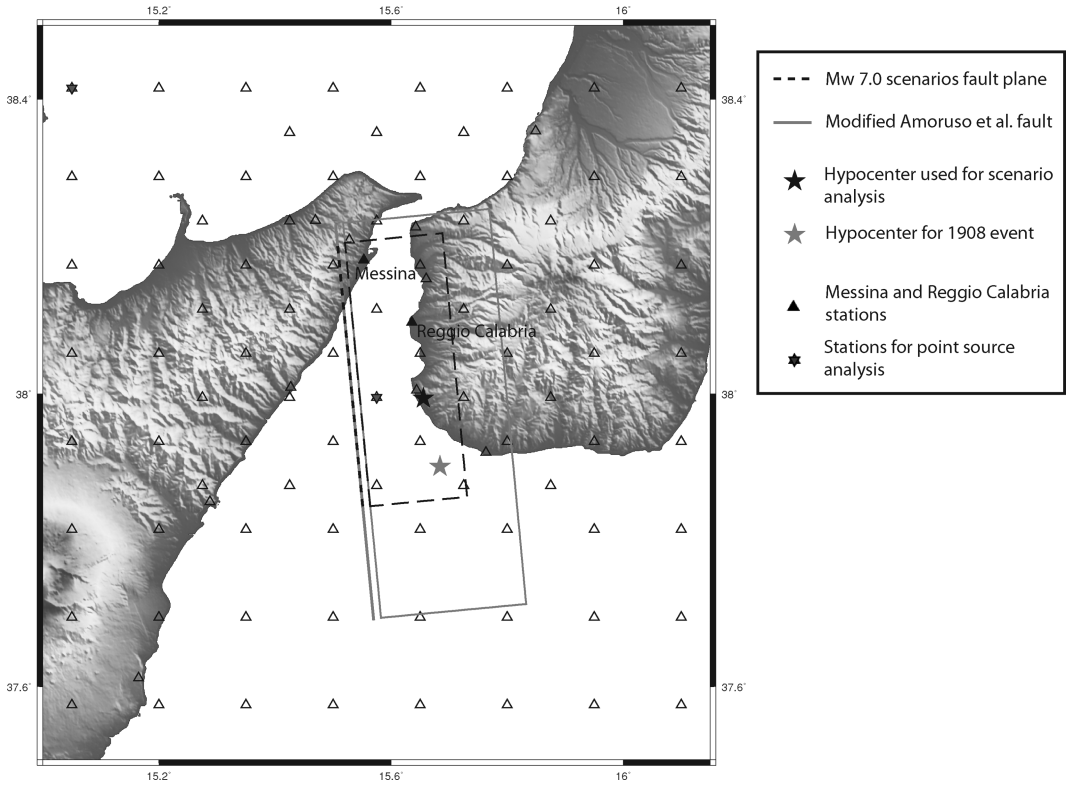

Figure 1. Stations (open triangles and closed hexagrams), hypocentres (stars) and surface projections of fault planes (dashed rectangles) utilized in this study. Dark grey dashed rectangle and dark grey star are referred to parametric M_w 7.0 scenarios, whereas light grey dashed rectangle and light grey star to the 1908 M_w 7.1 earthquake simulations.

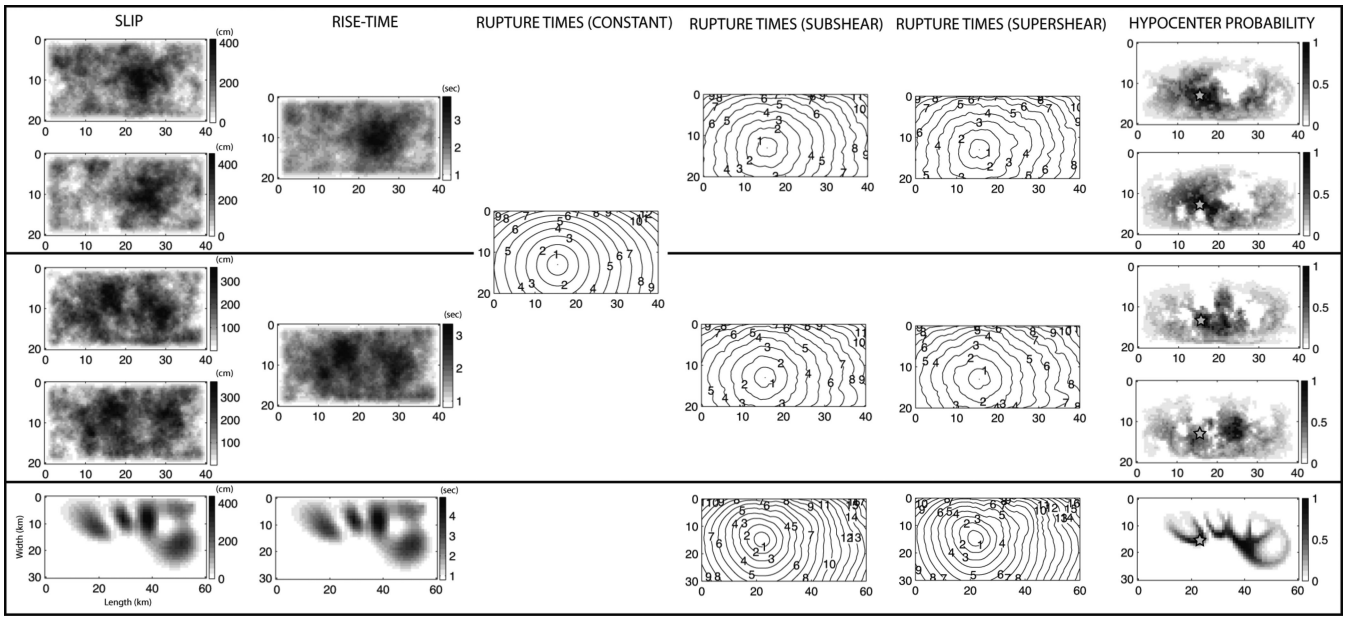

Figure 2. Rupture models developed in this study (see also Table 1 and 2) in terms of slip, rise-time and rupture propagation on the fault. First and second rows are referred to the M_w 7.0 scenarios, classified in single slip-patch (top row) and double slip-patch (centre row) models. Each of these rows contain two similar models to make our analysis more robust. The third row shows the 1908 M_w 7.1 event. The last column reports the normalized hypocentre probability distribution computed following Mai *et al.* (2005). Stars indicate chosen hypocentre locations. Rupture times contours are in seconds.

values (see Fig. 2 of Amoruso *et al.* 2006, for a comparison). The final slip model, rescaled to M_w 7.1, is shown in Fig. 2. It can be noted that a considerable part of the plane defining the fault is characterized by zero slip values. Although the original model was allowed to reach the surface, we force the top of the plane to lie at 1 km of depth as no clear evidence for surface breaking was found (Billi *et al.* 2008; Pino *et al.* 2009). Table 2 summarizes the corresponding fault parameters.

Slip distributions alone, as shown in Fig. 2, including the modified Amoruso model, do not specify a hypocentre. Instead of random or

Table 2. Fault plane and rupture models parameters for the 1908 M_w 7.1 earthquake. See text for details.

Fault	Source-time function	Rupture model
Strike : −5.5 ° Dip: 42.2 ° Rake: 242 ° Width : 30 km Length: 60 km	Boxcar	Variable rise-time–variable rupture speed (supershear)
Plane top: 1 km Plane bottom: 21 km	Yoffe	Variable rise-time–variable rupture speed (subshear)
Moment magnitude: 7.1		

complete arbitrary hypocentre selections, we pick its position based on the work of Mai *et al.* (2005), who examined the statistics of hypocentre locations for a large data set of published finite-fault models. The last column of Fig. 2 shows, for each slip model, the normalized probability of hypocentre position computed using the distribution functions proposed by Mai *et al.* (2005) and the chosen hypocentre itself (grey star). All random slip models share intentionally the same hypocentre location to better isolate ground-motion variability due to structural effects and the actual slip patterns. For these models, we fix the hypocentre to be in the southern section of the fault plane: this would likely correspond to the highest possible shaking levels on the Straits area (Fig. 1). We constrain the hypocentre to be in the southern part also for the modified Amoruso model because of evidences for south-to-north directivity effects for the 1908 event (Pino *et al.* 2009). Interestingly, the selected position based on the Amoruso slip-model and the findings of Mai *et al.* (2005) is in good agreement with that recently proposed by Michelini *et al.* (2005) after probabilistic first arrivals inversion. Hypocentres for the random slip and modified Amoruso models are reported also in Fig. 1.

3 VELOCITY MODELS

We use three distinct 1-D velocity models for the same area to include the influence of Earth structure uncertainty on ground-motions variability. These models have been recently proposed by different authors (Barberi *et al.* 2004; Langer *et al.* 2007) and are shown in Fig. 3. Although not referred as their best model, we consider also model 2 (model C in this paper) of Langer *et al.* (2007) to fully explore the crustal variability of the area under study. Except for model B (in dark grey), the others lack *S*-wave speed and density values. We, therefore, estimate shear-wave speed and density using the empirical relations proposed by Brocher (2005). The differences in the Earth models corroborate the structural complexity of the Messina Straits region. In particular, at depths less than 10 km, models A and B show a closely resembling pattern but with model A having lower velocities. Model C is instead characterized by a strong velocity contrast close to the surface. However, below a depth of 10 km, the velocity models are similar (Fig. 3).

4 PSEUDO-DYNAMIC APPROXIMATIONS

We utilize different kinematic rupture models in our investigation to explore the influence of Greens function variability. Besides simplistic approximations of the rupture process (i.e. constant rise-time

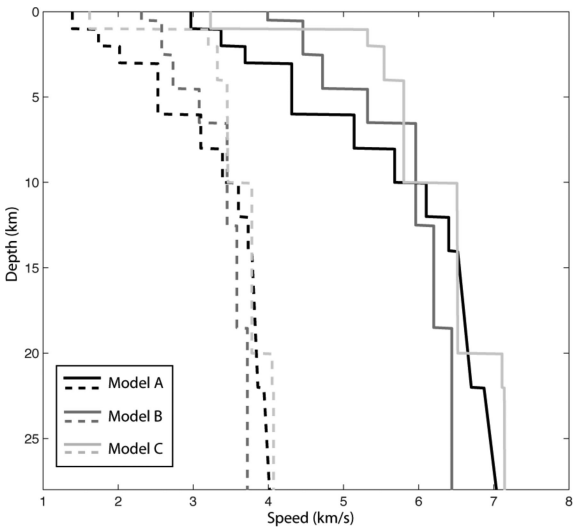

Figure 3. The three 1-D velocity models used in our simulations. Continuous lines represent *P*-wave speed, dashed lines *S*-wave speed. Black and light grey: models A and C, corresponding to model 1-D and model 2 of Langer *et al.* (2007). Dark grey: model B, from Barberi *et al.* (2004).

and rupture speed), we compute different scenario realizations by also varying rise-time and rupture speed consistently with spontaneous rupture models results (Day 1982; Oglesby & Day 2002; Pulido & Dalguer 2009). In detail, we allow for two rise-time and three rupture speed configurations, resulting in six cases: constant rise-time and constant rupture speed, constant rise-time and variable rupture speed (subshear), constant rise-time and variable rupture speed (locally super-shear), variable rise-time and constant rupture speed, variable rise-time and rupture speed (subshear), variable rise-time and rupture speed (locally super-shear). These source-model parametrizations are summarized in Table 1.

Rise-time variations $\Delta\tau$ with respect to a constant reference rise time are directly related to the particular slip distribution by the following relation:

$$\Delta\tau_{i,j} = \frac{\frac{1}{n}\sum_{k=1}^{n} D^k_{i,j} - \overline{\frac{1}{n}\sum_{k=1}^{n} D^k_{i,j}}}{\overline{\frac{1}{n}\sum_{k=1}^{n} D^k_{i,j}}}, \quad (1)$$

where $D^k_{i,j}$ represents the kth slip matrix that belongs to the same class (in this study $n = 2$), with i and j being the row and column indexes, respectively. The over-bar indicates averaging over the entire fault plane. Although dimensionless, we use the empirical quantity given in eq. (1) to assign a rise-time variation in units of seconds.

The dimensionless quantity expressed by eq. (1) can be added to an estimated average rise-time value $\bar{\tau}$ to give the final variable rise-time distribution

$$\tau_{i,j} = \bar{\tau} + \Delta\tau_{i,j}. \quad (2)$$

If desired $\Delta\tau$ can be scaled to assure final non-negative or user-defined minimum values, and to avoid unrealistic moment-rate peak values. Because $\Delta\tau$ has zero mean, the final rise-time distribution still maintains its original mean value, also showing a controllable range of variability. In this study, for all the source models including the modified Amoruso model, we assume an average rise-time $\bar{\tau}$ of 1.8 s, based on the scaling relation propose by Somerville *et al.* (1999). Final rise-time distributions are shown in the second column of Fig. 2. Obtained patterns resemble respective average

slip matrixes (first term of numerator in eq. 1). Basically, eq. (1) states that values on each point of the plane are proportional to the difference between the average slip matrix and its mean value. A similar approach, in which rise-time is proportional to slip, has previously been adopted by other investigators (e.g. Aagaard *et al.* 2008; Graves *et al.* 2008). Although dimensionless and scalable by the user, our parametrization of $\Delta\tau$ is more realistic than a purely random slip-uncorrelated rise-time distribution, because our approach encodes finding from source-dynamics studies that show how rise-time depends on slip and stress heterogeneity (e.g. Guatteri *et al.* 2003, 2004).

To track the propagating rupture front, we connect rupture speed variations to static stress-drop distribution as follows:

$$\overline{\Delta\sigma}_{i,j} = \frac{1}{n}\sum_{k=1}^{n}\Delta\sigma_{i,j}^{k}, \tag{3}$$

where $\Delta\sigma_{i,j}^{k}$ is the stress-drop matrix computed for the kth slip model belonging to the same class using the procedure described in Ripperger & Mai (2004). Stress-drop distributions obtained from variable slip on the fault are highly heterogeneous, characterized by regions of positive and negative stress drop, as demonstrated by Bouchon (1997). From the obtained average stress-drop distribution $\overline{\Delta\sigma}$, we compute the mean negative and mean positive stress-drop values along with their weights w_i:

$$\begin{aligned} w_1 &= \text{num}\left\{\overline{\Delta\sigma}_{i,j} > \text{mean}\left(\overline{\Delta\sigma}_{i,j}^{+}\right)\right\} \\ w_2 &= \text{num}\left\{\overline{\Delta\sigma}_{i,j} < \text{mean}\left(\overline{\Delta\sigma}_{i,j}^{-}\right)\right\} \\ w_3 &= \text{num}\left\{\text{mean}\left(\overline{\Delta\sigma}_{i,j}^{-}\right) \geq \overline{\Delta\sigma}_{i,j} \leq \text{mean}\left(\overline{\Delta\sigma}_{i,j}^{+}\right)\right\}. \end{aligned} \tag{4}$$

Here the +/- superscript indicates positive/negative stress-drop values, respectively, whereas the num-operator returns the number of matrix elements satisfying the specified condition. At this point, we impose the rupture speed to assume a given mean value ($0.75*\beta$) only where condition for w_3 is met, and we assign the maximum value ($0.9 * \beta$) where condition for w_1 is met. These rupture speed values (in percent of the *S*-wave speed) are determined using a trial-and-error approach. The minimum value is then computed using weights w_1 and w_3, to assure that the mean rupture speed reaches at the desired value.

The described procedure produces faster rupture velocities in areas characterized by higher-than-average stress drop. If we allow for locally super-shear speed, the workflow features two more steps: we force the rupture speed to be super-shear ($1.5 * \beta$) where the 95th percentile of $\overline{\Delta\sigma}^{+}$ is exceeded, and then assign a particularly low value where the 5th percentile of $\overline{\Delta\sigma}^{-}$ is not exceeded. As before, this low value is computed to guarantee a mean speed value close as much as possible to the desired one. The above procedure is based on the assumption that faster rupture speeds are observed in region of high stress drop (Day 1982). Moreover, although simplistic and based on a trial-and-error procedure, our approach reflects recent evidences about high-frequency generation mainly within large stress-drop regions (Pulido & Dalguer 2009).

To avoid any influence of the different media characteristics on the source characterization, we compute the actual rupture times using a common minimum-velocity model, obtained by selecting the slowest wave speed at each depth level. As can be noted from Fig. 3, it corresponds to model A for the first ten kilometres and to model B at deeper levels. Computations of rupture front arrivals are then carried out, for each slip-class, by applying a ray-tracing (i.e. rupture-front tracking) algorithm (Hole 1992). Following this procedure, we insure that absolute rupture speed values are the same for each rupture speed class. As an example, in Fig. 4 we report the on-fault relative rupture speeds for the single slip-patch case. Both constant and variable rupture speed cases are shown. According to crack dynamics studies (Andrews 1976; Dunham *et al.* 2003) and laboratory experiments (Rosakis *et al.* 1999, 2006), shear cracks cannot propagate at speed Cr between $0.92 * \beta < Cr < \beta$ (considering mixed mode II and III). In this study, we obtain rupture speed in this forbidden regime only for small sections of the fault plane for super-shear cases related to velocity models B and C. However, considering their negligible extent (less than 0.1 per cent of fault surface), we believe that they have no effect on the overall physical validity of our models.

Finally we apply three different source-time functions: boxcar, triangular and the modified Yoffe function proposed by Tinti *et al.* (2005). For the latter, a constant acceleration time ('Tacc' in Tinti *et al.* 2005) of 0.33 s has been adopted. This value would correspond to the minimum resolvable period in our deterministic simulations. Table 1 and 2 summarize the source model characteristics used in all our simulations.

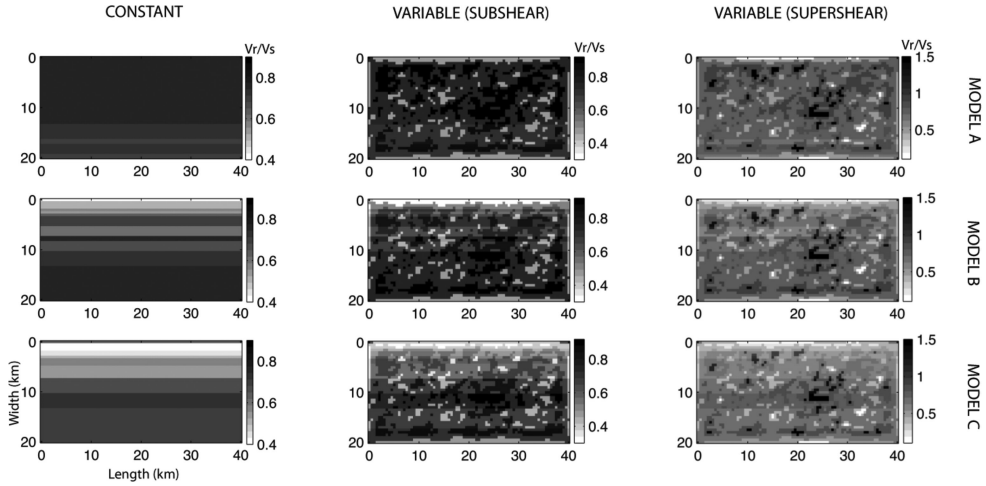

Figure 4. Ratios of rupture speed versus shear wave speed for the single slip-patch case and the three velocity models considered. Non-physical rupture speed values ($0.92 * \beta < Cr < \beta$) for the super-shear case (last column) due to the pseudo-dynamic modelling approach constitute less than 0.1 per cent of fault surface, and are insignificant for the seismic radiation.

Considering three velocity models, four random-slip models and variability in source-time function, rise-time and rupture speed, we simulate ground motions for a total of 216 scenarios in the Messina Straits area.

5 BROAD-BAND WAVEFIELD COMPUTATION

The low-frequency (LF) deterministic synthetics are computed using a discrete wavenumber technique (COMPSYN, Spudich & Xu 2003) up to a maximum frequency of 3.0 Hz. We set this frequency considering its resolving power compared to the average thickness of layers characterizing our velocity models. Because COMPSYN calculations are referred to perfectly elastic media, we approximate *S* body wave attenuation for the deterministic LF-synthetics through a $t*$-operator that depends on traveltime and quality factor Q (Varela *et al.* 1993). *S*-waves traveltimes for each medium are computed using a ray-tracing algorithm (Hole 1992).

To compute the $t*$-operator, we consider a quality factor model of the form:

$$Q = Q_0 f^{\alpha}. \tag{5}$$

Because our velocity models are different in the shallower part (less than 10 km), we compute different values of Q_0 for each of them. These values are estimated using the relation

$$Q_0 = 50 V_S, \tag{6}$$

proposed by Graves *et al.* (2008) for computing near-field seismograms up to 1 Hz in southern California, a tectonically active region. Although developed for a specific region, this equation can be applied to our case study that involves a tectonically very active area of ongoing deformation and a continuously high level of seismicity. We, thus, express the differences in attenuation for the three crustal models using eq. (6), limiting our calculations to the first 10 kilometres of depth. We obtain Q_0 values of 115, 140 and 155 for models A, B and C, respectively.

The frequency-decay parameter α is assumed to be 0.8 after a trial-and-error procedure to reproduce the distance-decay rate of simulated PGV values with respect to empirically predicted by attenuation relations of Boore & Atkinson (2008) and Campbell & Bozorgnia (2008). Following several studies (see Sato & Fehler 1994, p.114), we keep the quality factor constant up to 0.5 Hz and then let it increase following the exponential of eq. (5).

We calculate hybrid broad-band synthetics using the method developed by Mai *et al.* (2010). It permits to merge stochastic high-frequency seismograms to pre-computed LF-synthetics around a specified matching frequency. The stochastic high-frequency seismograms are based on multiple S-to-S scattering theory (Zeng *et al.* 1991; Zeng 1991, 1993). For all cases, we use the Dreger source time function to compute high-frequency contributions avoiding unrealistic spectral notches (Mena *et al.* 2010). Coda wave attenuation is explicitly handled in the stochastic component by assuming the exponential form of eq. (5): in this case, we use the same Q_0 values as specified for the deterministic synthetics but a slightly different frequency-decay parameter α, set to 0.7 after a trial-and-error procedure, to obtain PGA decay rates closer to those predicted by empirical relations. The matching frequency is set at 2.0 Hz, thus falling in the transition between the deterministic and stochastic near-field seismic radiation, thought to be in the range 1–4 Hz (Pulido & Kubo 2004).

The generic GMPE-based attenuation models discussed above for direct and coda waves are characterized by values constantly higher than those estimated by Tuvé *et al.* (2006) for the Messina Straits area (see Table 3). Hence, for each velocity model, we first halve previous Q_0 values and then estimate new frequency-decay parameters by fitting the attenuation models proposed by Tuvé *et al.* (2006) for both direct and coda waves. Obtained values are listed in Table 3. Although arbitrary, this approach allows us to obtain more representative attenuation models of this complex tectonic region, without omitting differences of the velocity profiles. In the following, we adopt the generic GMPE-based attenuation models (higher Q_0 values; second column of Table 3) to analyse ground-motions variability and to verify the validity of our simulations; in contrast, the specific attenuation models (lower Q_0 values; third column of Table 3) are used to compute past (M_w 7.1, 1908 earthquake) and future (M_w 7.0) scenarios. Scattering and absorption coefficients values are the same for both models and are estimated from the work of Tuvé *et al.* (2006).

Table 3. Attenuation models for the 1-D velocity structures used in our simulations. Direct *S*-waves values are used for the deterministic low frequencies, whereas coda waves values for the stochastic high-frequency computations. Values estimated by Tuvé *et al.* (2006) for the Messina Straits area are reported in the first column.

	Tuvé *et al.* (2006)	GMPE fit	Tuvé *et al.* (2006) fit
Direct *S*-wave attenuation	$Q = 61 * f^{0.7}$	$Q = 115 * f^{0.8}$	$Q = 60 * f^{0.77}$
Coda waves attenuation	$Q = 76 * f^{0.5}$	$Q = 140 * f^{0.8}$ $Q = 155 * f^{0.8}$ $Q = 115 * f^{0.7}$ $Q = 140 * f^{0.7}$ $Q = 155 * f^{0.7}$	$Q = 70 * f^{0.6}$ $Q = 80 * f^{0.5}$ $Q = 60 * f^{0.66}$ $Q = 70 * f^{0.55}$ $Q = 80 * f^{0.49}$

6 STATISTICAL ANALYSIS OF GROUND MOTIONS

We first carry out a test involving a point source to assess the particular response of each velocity model to simple forces. Here, our attention is focused only on the LF deterministic component of the ground-motion, because the high-frequency part is essentially stochastic and hence unrelated to the media response. Synthetics are computed for an M_w 3.6 normal-faulting earthquake at a depth of about 9 km (dark-grey star in Fig. 1), characterized by a boxcar source time function with rise-time of 0.3 s. In Fig. 5, we present synthetics for two stations (indicated by hexagrams in Fig. 1), one close to the epicentre and one in the far north-west corner of the computational domain, after the t*-operator has been applied to include attenuation. As can be noted, model A synthetics (in black, as in Fig. 3) show the highest amplitudes. This can be explained by the lower shear wave speed (in the upper ten kilometres) that also generates pronounced surface waves at large epicentral distances (Fig. 5b). For the other two velocity models surface waves are not or barely developed. Model B (dark grey) is characterized by slightly higher wave amplitudes than model C (light grey). Although the synthetic seismograms for the station closer to the source (Fig. 5a) are rather similar to each other, those related to model A contain longer pulses. This can be explained by the higher *Vp*/*Vs* ratios characterizing this model, in particular in the shallowest layers (Fig. 3).

Next, we analyse our broad-band simulations for random slip models by comparison with the NGA (http://peer.berkeley.edu/nga/)

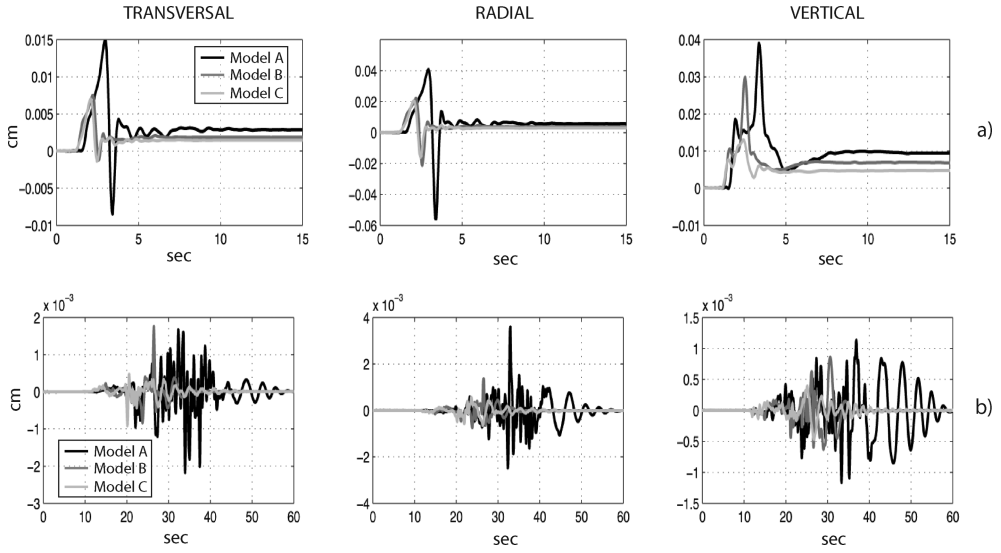

Figure 5. Displacement synthetics for the three 1-D velocity models at two stations produced by a dip-slip M_w 3.6 point source, located at about 9 km of depth and characterized by a boxcar source-time function (rise-time of 0.33 s). Maximum frequency is 3.0 Hz. Source (dark grey star) and receivers (hexagrams) locations are shown in Fig. 1. Top row: receiver close to source. Bottom row: receiver far from source.

relations of Boore & Atkinson (2008) and Campbell & Bozorgnia (2008). In addition, we compare our results against predicted values by computing residuals through the following expression:

$$\overline{R} = \frac{1}{n}\sum_{i=1}^{n}\left[\ln\left(\overline{Y}\right)_{i,\mathrm{sim}} - \ln\left(Y\right)_{i,\mathrm{pred}}\right], \tag{7}$$

where n is the number of stations used and Y is the considered parameter (PSA, PGV or PGA in this work). Note that $\overline{Y}$ indicates, for the ith station, the parameter averaged over a given number of simulations (gathered according to specific criteria, see below). Positive values of $\overline{R}$ correspond to larger than predicted ground-motion levels, whereas negative values indicate lower than predicted ground-motion levels. When considering a single simulation, eq. (7) corresponds to formulas 3.1 and 3.2 of Star *et al.* (2008).

In Fig. 6, we display the results for all 216 scenarios and the two attenuation models used in this study. The figure reports computed PGA and PGV values and the corresponding empirical predictions, as well as the residuals (as given by eq. 7 considering all simulations). Although the Boore & Atkinson (2008) model is chosen for distance plots due to its simplicity, we prefer the Campbell & Bozorgnia (2008) relation for analysing residuals because it distinguishes between hangingwall and footwall stations. These summary figures exhibit important general features of our simulations: large ground-motion variability at each distance range, with higher than predicted values at long periods contrasting lower than predicted values at short periods. This can be traced back to the coherency of our slip models, that also controls variations of rise-time and rupture speed: smooth (coherent) rupture favour long-period radiation at the expense of diminished high-frequency radiation due to small-scale source complexity. Note also that our attenuation models based on the findings of Tuvé *et al.* (2006) (third column of Table 3) results in faster decay rates than expected, especially at short periods and large distances.

In Fig. 7, we carry out our residuals analysis at multiple levels investigating the influence of velocity models relative to the source-time functions. In Fig. 7(a), showing results separately for each velocity model, residuals have been computed considering parameters averaged ($\overline{Y}$ term in eq. 7) over source-time functions and slip classes. In Fig. 7(b), dedicated to source-time functions, the averaging process involves velocity models and slip classes. In each figure, rows describe the simulation residuals for different rupture models indicated by indexes ranging from 1 to 6: these indexes and the relative rupture models are reported in the last column of Table 1.

As one could expect from Fig. 5, velocity model A gives the largest values for all considered parameters (PGV, PGA and PSA). Although more appreciable at short periods, differences associated to velocity models remain important also at long periods and are rather insensitive to the particular rupture model adopted (Fig. 7a). Differences at very long periods can be related to the mechanical properties (i.e. rigidity) of each velocity model. This can be noted also from the static displacements shown in Fig. 5(a). On the other hand, the ground-motion variability due to different source time functions is more intricate, showing dependency on period and rupture model. The boxcar, triangular and Yoffe source-time functions, as already pointed out by Mena *et al.* (2010), show peculiar spectral characteristics that can be reflected in simulated ground motion. As depicted in Fig. 7(b), at intermediate and long periods ($T > 2$ s) the Yoffe and the triangular source-time functions consistently show the largest values. On the contrary, the latter is always associated to the lowest values at shortest periods ($T < 0.5$ s). In this domain, the boxcar and Yoffe source-time functions give about the same ground-motions levels when variable rise-time and variable rupture speed models are used.

Moreover, the effects of variable rupture speed and, secondarily, variable rise-time can be clearly outlined: although long periods are insensitive to these variations, high frequencies are sufficiently excited only if a pseudo-dynamic approach is pursued (Figs 7a and b, rupture models 2 to 6). This behaviour is also strongly visible in the PGA residuals. PGV is instead less affected, showing in every case rather stable values. Another interesting point concerns the standard deviations for each single item of Figs 7(a) and (b): a careful analysis leads to the observation that, for short periods, variable rupture speed (in particular for the super-shear case; Figs 7a and b, rupture model 3 and 6) increases the standard deviation whereas variable rise-time reduces it. At long periods, this behaviour is again no longer visible. This can be explained by the fact that in our

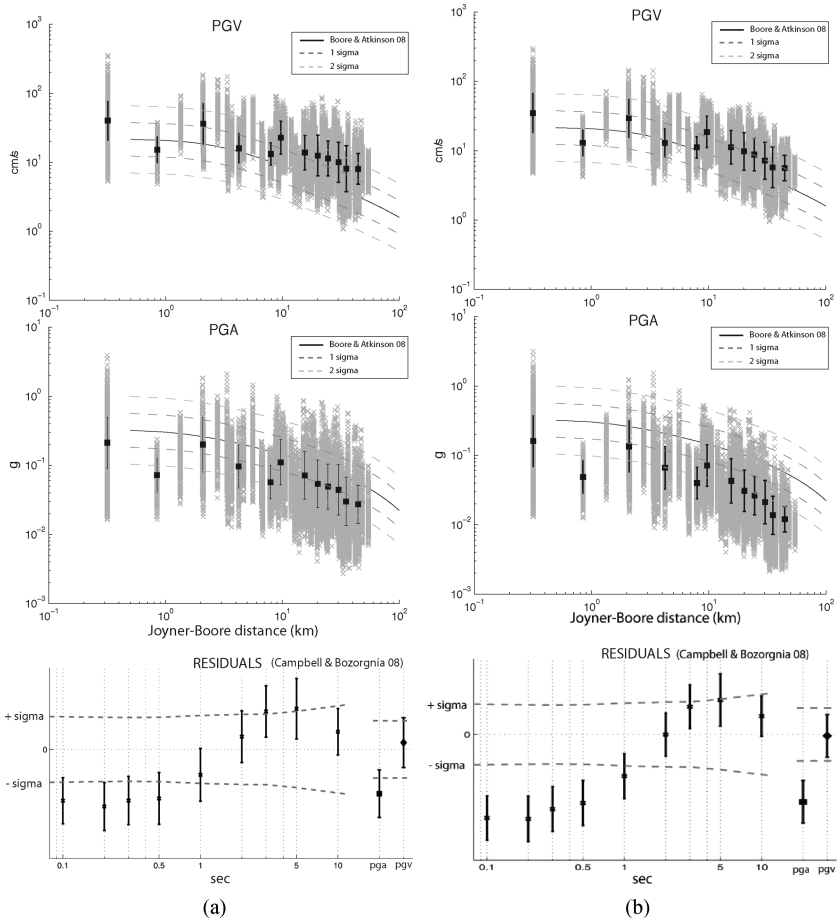

Figure 6. Plots showing all the M_w 7.0 simulations for two different attenuation models (left-hand side: GMPE fit; right-hand side: Tuvé *et al.* 2006, fit; see Table 3). First and second row: synthetics PGV and PGA against Boore & Atkinson (2008) predicted peak ground motions; mean values and population standard deviation are represented by black squares and vertical lines. Bottom row: residuals for PGA, PGV and PSA at different periods computed with respect to the Campbell & Bozorgnia (2008) empirical relation; mean value and standard deviation are shown.

pseudo-dynamic approach rupture speed variations are important at short scales whereas rise-time, being proportional to slip, tends to contrast peak slip velocity variability over the fault plane.

In Fig. 8, we report standard deviation for each triplet of Figs 7(a) and (b). Its computation is based only upon the three mean values of the triplets, because we are interested in evaluating the variability induced by structure and source. The different rupture process approximations at each period are distinguished by numbers (see Table 1) to better illustrate their relative importance for ground-motions variability. The medium-related variability trend (squares in Fig. 8) is clearly visible, remaining rather constant over the whole spanned period range, while the source-time function influence (circles in Fig. 8) is strong at short to intermediate periods and then drops to very low levels at long periods. As noted previously, different rupture approximations assume an important role, considering also different source-time functions; the analysis in Fig. 8 corroborates our earlier finding that the greatest variability is associated to variable rupture speed cases. More general, examining carefully the different trends for standard deviation, we find that ground motions variability is clearly dominated by source terms at short periods, whereas at periods longer than 3 s it is controlled by velocity models differences. Similar behaviour is found also for PGV and PGA. This may imply that, although source processes represent undoubtedly the main factor influencing ground motions at short and intermediate periods, also structural uncertainties should be included in scenario simulations to fully explore possible shaking variability levels.

An analogous residuals analysis in two different distance ranges (from 0 to 30 Km and from 30 to about 60 Km) reveals no pronounced distance-dependence. For brevity, we omit in Fig. 7 the residuals analysis for slip classes (where the averaging is over velocity models and source-time functions) also because in this case no particular trends are visible. This observation indicates that globally these two classes are equivalent in terms of ground motions, whereas angular dependences are to be expected as well as local differences due to the radiation pattern.

It is important to note that that each entry in Fig. 7 is the result of an averaging process over several quantities: for instance, entries in Fig. 7(a) are the result of averaging simulations featured by different source-time functions and slip classes. As such, these residuals estimates are valid for a wide range of cases, and are not restricted to a single scenario. Therefore, Fig. 7 implies that small residuals at short periods are obtained only when pseudo-dynamic approximations are used. In that case, with the Yoffe function returning the best results, it is interesting to note that the triangular source-time function is unable to reproduce satisfactory PGA and PSA values due to its spectral content depleted in high frequencies. Simple standard kinematic modelling (i.e. constant rise-time and

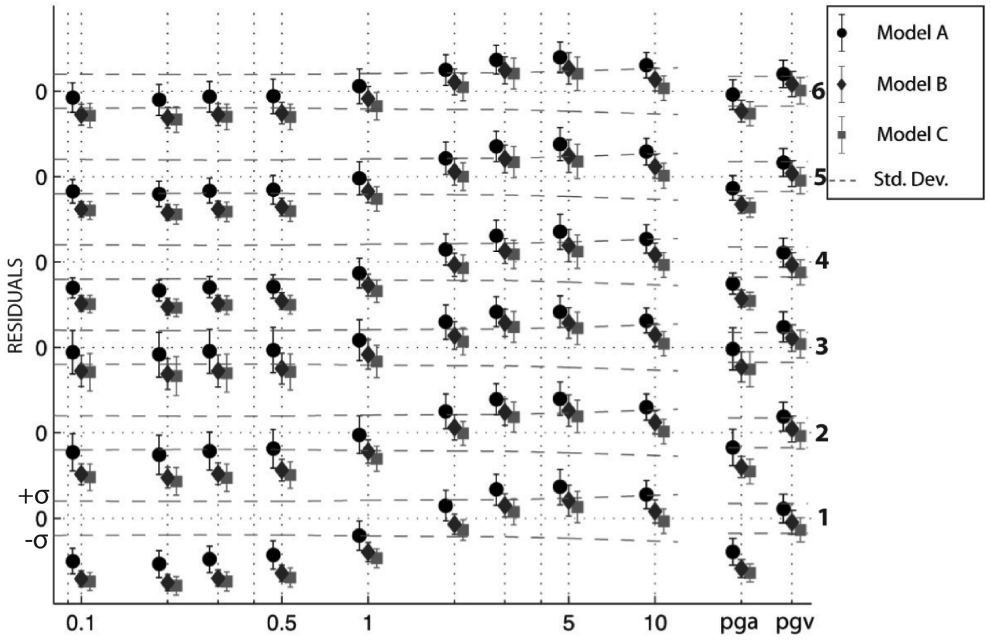

(a)

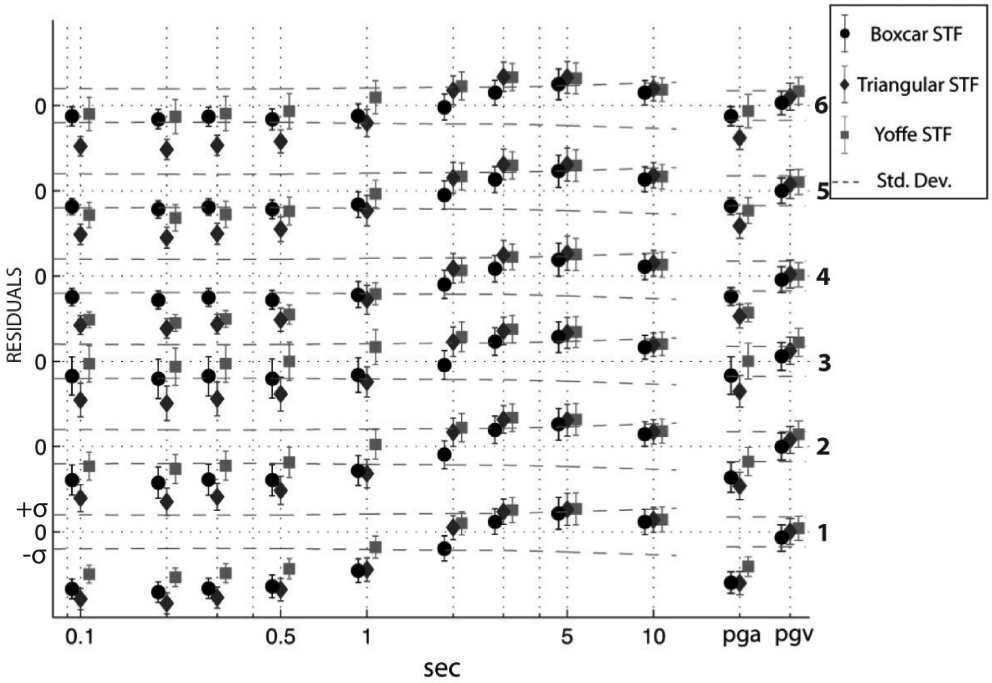

(b)

Figure 7. (a) Residuals for synthetics PGA, PGV and PSA at different periods with respect to the Campbell & Bozorgnia (2008) attenuation relation. Only M_w 7.0 simulations are used. Entries shown are mean value and standard deviation; the zero-labelled dotted line indicates unbiased estimations, whereas the dashed grey line represents one standard deviation. Each row describes residuals for different rupture models as indicated by numbers from 1 to 6 on the right-hand side (see last column of Table 1 for reference). Residuals are computed after grouping simulations with respect to different velocity models. (b) Same as for Fig. 7(a), but with residuals computed after grouping simulations with respect to different source-time functions.

constant rupture speed) always results in unrealistic modelling of PGA and short-period PSA, regardless of source-time function or velocity model used.

On the other hand, velocity model A gives the lowest residuals while models B and C present residuals often too high at short periods. However, it has to be considered that our rupture models are tailored to a common reference velocity model equal to model A for the first 10 km (where the largest part of the rupture process occurs). As can be noted from Fig. 4, this methodology has the inconvenience of generating relatively low-rupture velocities (compared to local shear wave speed) over large sections of fault surface for velocity models B and C. This feature may be partly responsible for the constant underprediction of PGA and PSA values for these two velocity models.

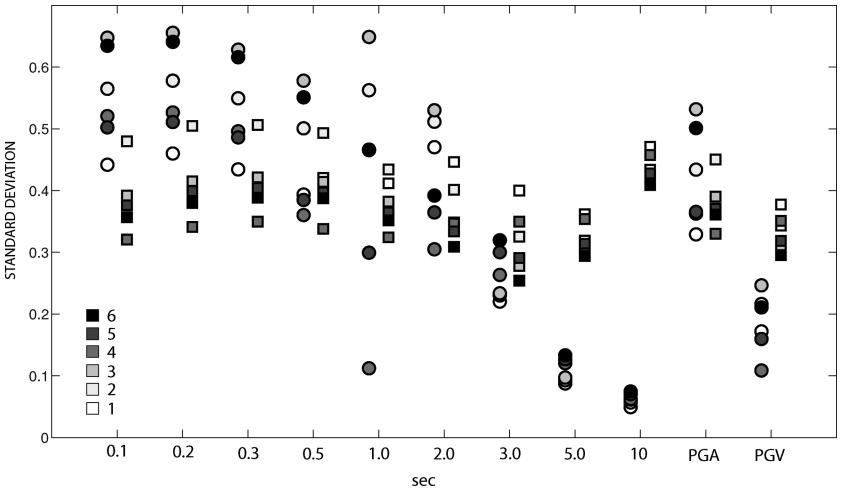

Figure 8. Standard deviation computed at each period over the three mean values constituting the triplets of Figs 7(a) and (b). Squares refer to velocity models group (Fig. 7a), circles to source-time functions group (Fig. 7b). Numbers from 1 to 6 indicate different rupture models as reported in the last column of Table 1.

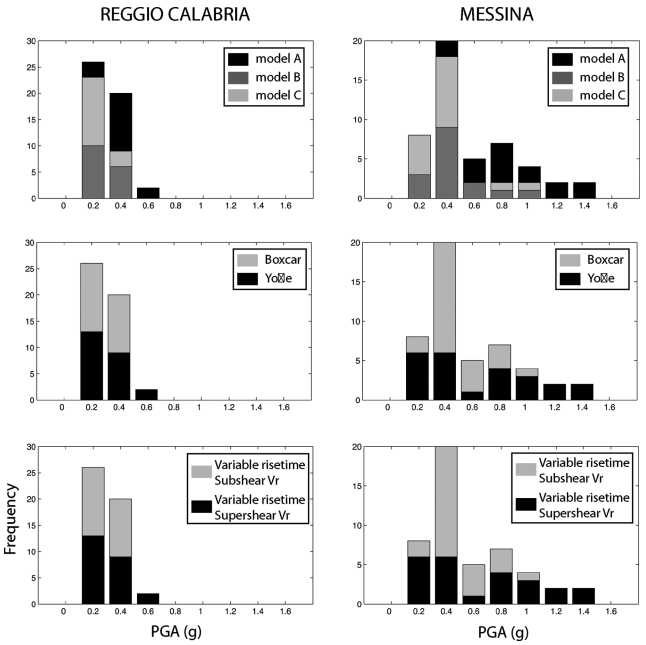

Figure 9. Histogram representations of PGA for the cities of Reggio Calabria and Messina for some of the simulated M_w 7.0 events (see text). Site amplification factors are based on Vs30 values. Contributions in terms of velocity models (first row), source time functions (second row) and rupture models (third row) are shown.

Focusing our attention on the most important cities in the Straits area, Messina and Reggio Calabria, we examine corresponding PGA values (Fig. 9). Following the above observations, we keep only those simulations giving the most satisfying levels of fit with respect to ground-motions prediction equations. This subset consists of variable rise-time and variable rupture speed (subshear) and variable rise-time and variable rupture speed (locally super-shear) models. Moreover, although all velocity models are used, we keep only boxcar and Yoffe source-time functions, and use the specific attenuation model (third column of Table 3) derived from the work of Tuvé *et al.* (2006) which result in faster decay rates.

Simulations considered so far are referred to hard rock soils and hence do not account for local site and non-linear soil effects near the surface. For this reason, we apply a site-amplification correction to this subset of synthetics, using a methodology proposed by Graves & Pitarka (2004) based on Vs30 values and recently adopted also in Mai *et al.* (2010). In this approach, the response-spectral amplification factors of Borcherdt (1994, 2002) are applied in the Fourier domain to scale the amplitude spectrum. Vs30 values of 400 m s^{-1} for the Messina city and 373 m s^{-1} for the Reggio Calabria city are extracted from the USGS Vs30 global maps based on topographic slope (Allen & Wald 2007). Results in Fig. 9 are shown in histograms separating the influence exerted by medium, source-time function and rupture model. According to our simulations the largest peak values occur in the city of Messina, where PGA values of 1 g or higher may be expected. For Reggio Calabria our simulations predict lower peak accelerations, not exceeding 0.6 g.

7 SIMULATIONS OF THE 1908 M_W 7.1 MESSINA STRAITS EARTHQUAKE

To study the ground-motion pattern of the 1908 M_w 7.1 Messina Straits earthquake and to compare observations with simulation, we use the same rupture models and source-time functions as for Fig. 9 (see also Table 2) and the modified Amoruso slip model (see bottom row of Fig. 2). We utilize all three velocity models considered in this study, and apply our specific attenuation model (third column of Table 3) derived from Tuvé *et al.* (2006). Fig. 10 shows plots of synthetics PGA and PGV from all simulations (not accounting for site amplification at this stage) against those predicted by the Boore & Atkinson (2008) empirical relation. Residuals for PGA, PGV and PSA at several periods with respect to the Campbell & Bozorgnia (2008) predictions are reported as well.

The ground motions displayed in Fig. 10 resemble the pattern in the right-hand column of Fig. 6 (for M_w 7.0 simulations): underpredicted values at short periods and fast decay rates for PGA. This behaviour can be related to the particular, patchy slip model and the notably high-attenuation values characterizing this tectonically complex area (Tuvé *et al.* 2006). When we focus on the resulting PGA values for the cities of Messina and Reggio Calabria (Fig. 11) after including site-amplification corrections, we observe a different behaviour with respect to that encountered in Fig. 9: in this case no differences are visible between the two cities, and the highest peak

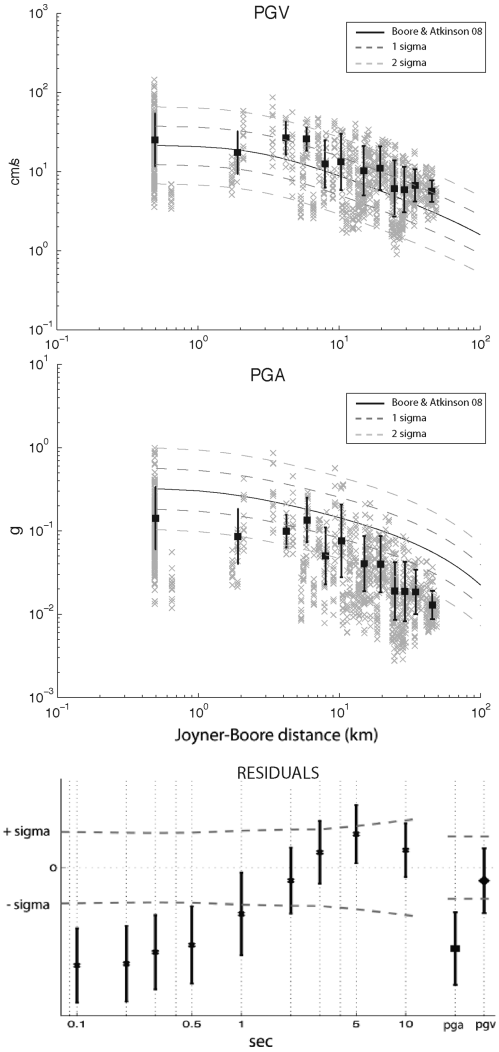

Figure 10. Plots showing all simulations results for the 1908 M_W 7.1 Messina Straits earthquake (see Table 2). Only the Tuvé *et al.* (2006)-based attenuation model has been used (Tuvé *et al.* 2006, *fit* of Table 3). Top and central panel: synthetics PGV and PGA from our broad-band simulations against Boore & Atkinson (2008) predicted peak ground motions; mean value and population standard deviation are represented by black squares and vertical lines. Bottom panel: residuals for PGA, PGV and PSA at different periods respect to the Campbell & Bozorgnia (2008) empirical relation; mean value and standard deviation are shown.

values are around 0.6 g. Fig. 12 displays example time-series of two broad-band ground-motion for Messina and Reggio Calabria.

Finally, we compare simulated ground motions for the 1908 event against available macroseismic intensities maps. For this purpose, we apply site amplifications factors to all receivers on land and compute average PGA values using all simulations (Table 2). However, we do not estimate macroseismic intensities from PGA through available empirical relations (e.g. Wald *et al.* 1999) because we are primarily interested in a direct geometrical comparison. Moreover, macroseismic intensities are strictly related to masonries quality and also to site and particular 3-D wave-propagation effects that are not considered in our simulations, hence a quantitative comparison could be misleading. Our PGA map and a representative smoothed MSK map for the 1908 event (Bottari *et al.* 1986) are compared in Fig. 13: although our map shows a pattern roughly symmetrical with respect to the Straits axis, the isoseismals map reports higher

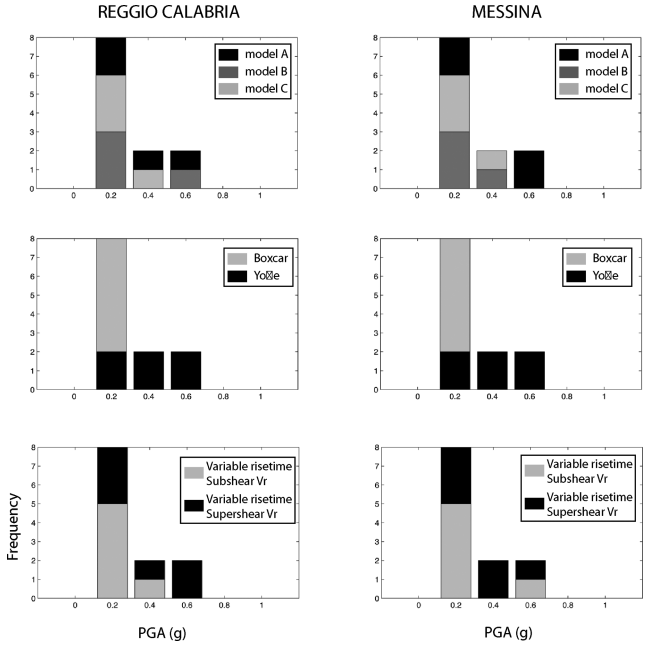

Figure 11. Histogram representations of PGA for the cities of Reggio Calabria and Messina as obtained from the 1908 M_W 7.1 Messina Straits event simulations. Site amplification factors are based on Vs30 values. Contributions in terms of velocity models (first row), source-time functions (second row) and rupture models (third row) are shown.

damage levels in the Calabria region (east of the Messina Strait). These differences are likely due to the fact that our simulations consider only a single hypocentre position and do not account for 3-D basin effects that strongly affect the resulting wavefield.

8 CONCLUSIONS

In the context of broad-band scenario simulations for M_W 7.0 events in the Messina Straits region, we compare the influence of three available 1-D velocity models (Barberi *et al.* 2004; Langer *et al.* 2007) on ground-motions levels with respect to source-related variability. The faulting process is approximated through a sequence of simple kinematic and more realistic pseudo-dynamic models affecting rise-time and rupture speed. Two basic classes of random slip distributions are generated using the procedure of Mai & Beroza (2002): one-patch and two-patch slip models. The local on-fault slip-rate function is described using boxcar, triangular and modified Yoffe (Tinti *et al.* 2005) source-time functions. For the latter, a constant acceleration time of 0.33 s is assumed. We use a fault plane whose location, orientation and mechanism are derived directly from a recent source-model study (Amoruso *et al.* 2006). Their particular source geometry differs from that proposed in the Italian database of individual seismogenic sources (Basili *et al.* 2008), but it is corroborated by modelling results using all available geophysical data (Amoruso *et al.* 2006). We, thus, choose this rupture plane model in our study, also for investigating the ground-motion pattern of the 1908 M_W 7.1 earthquake.

In our work, the adopted crustal models are characterized by velocity profiles whose properties are markedly different in the upper 10 km of the Earth crust, where a large part of the rupture process takes place. Broad-band synthetics are generated using the hybrid method proposed by Mai *et al.* (2010). Attenuation is included through two models, one generic and the other specific for the Straits region (Tuvé *et al.* 2006).

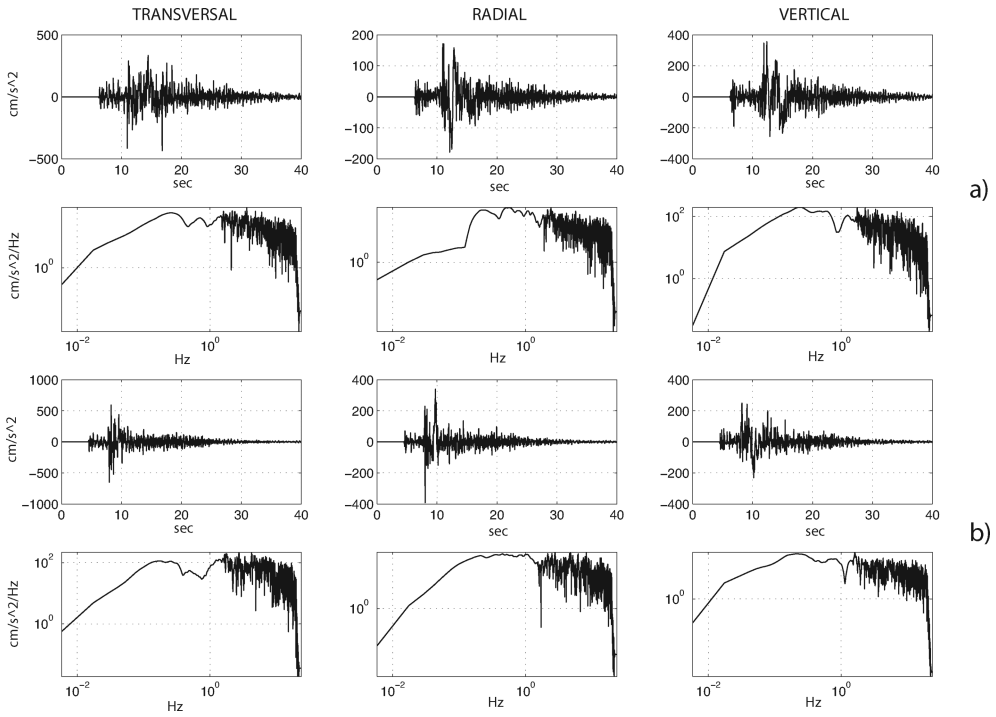

Figure 12. Broad-band synthetic seismograms for the cities of Messina (a) and Reggio Calabria (b) referred to the 1908 M_W 7.1 Messina Straits event simulation using velocity model B, Yoffe source-time function and variable (super-shear) rupture speed.

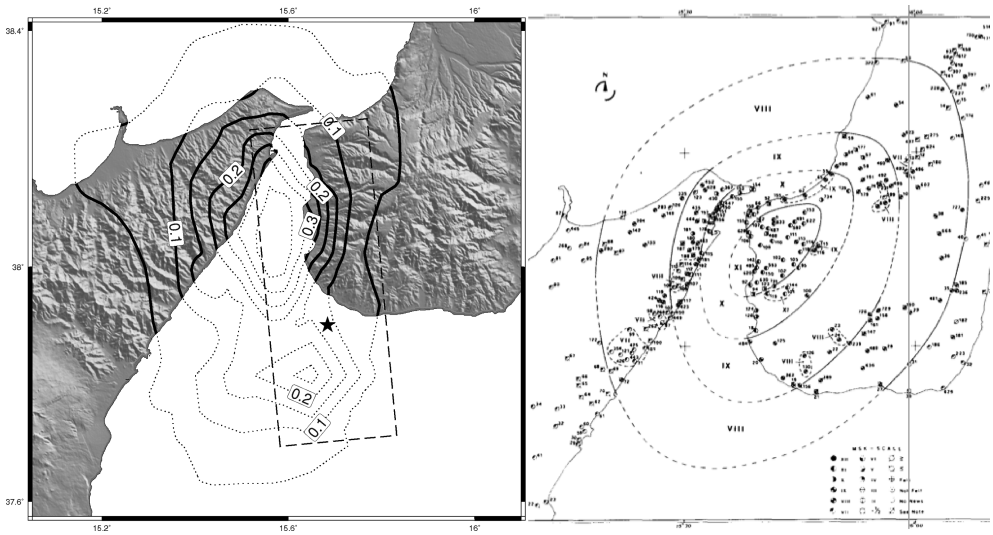

Figure 13. Left-hand side: contour plot showing average PGA values (in g) as derived from our 1908 M_W 7.1 Messina Straits event simulations. Contour spacing is 0.05 g; both fault plane projection and epicentre are shown. Right-hand side: MSK contour map reported in Bottari *et al.* (1986).

We compare our simulations against the empirical attenuation relations of Boore & Atkinson (2008) and Campbell & Bozorgnia (2008). Chosen ground motion intensity measures are the PGV, PGA and spectral acceleration (5 per cent damping). We find that our simulations are generally in good agreement with empirically predicted values when the generic attenuation model is used. Interestingly, each simulation shows an overall pattern represented by slight over-prediction trend at long periods and slight under-prediction trend at short periods (Figs 6, 7a and 7b). A similar behaviour has been reported also in Graves *et al.* (2008). Considering that our broad-band technique remains unchanged for all the rupture models, we conjecture that this pattern of over- and under-prediction is related to the coherency of our slip models, that also influences variations of rise-time and rupture speed (see eqs 1 and 3). Supplementary simulations carried out at a maximum frequency of 20 Hz show no significant PGA and SA changes when an intrinsic attenuation model is used. Because we are using heterogenous slip distributions, characterized by one or two high-slip areas, ground-motion residuals at long periods do not show significant variability, whereas short period variability is strictly dependent on the faulting process approximation (Figs 7a and b).

Classic kinematic models and triangular source-time function always underestimate ground shaking levels at periods shorter than 1–0.5 s. On the other hand, we find that contributions to

high-frequencies radiation are controlled mainly by variable rupture speed and secondarily by variable rise-time, indicating that only pseudo-dynamic approximations can reproduce realistic broad-band ground motions. Analogous observations can be found in a recent study by Cultrera *et al.* (2010). At the same time, rupture speed variability is able to increase ground-motion variability; an opposite effect is encountered for rise-time, due to its proportional dependence on slip. In contrast, variability due to Greens functions uncertainty is common over all periods. Even if less important at high frequencies, where source-driven effects appear to dominate, it becomes notable for longer periods. Although our results show slight dependencies on the specific velocity models, we conclude that the main factor affecting ground motions variability at high frequencies is represented by the source term. However, at intermediate and (especially) long periods uncertainties, details of crustal structures become important and should, therefore, be included in broad-band simulations.

Considering only those simulations that adequately reproduce empirically predicted shaking levels and applying site amplification factors based on Vs30 estimations (Graves & Pitarka 2004; Mai *et al.* 2010), we show that for possible future M_w 7.0 events the city of Messina could experience ground-motions peak levels exceeding gravitational acceleration (PGA >1 g). Lower levels, around 0.6 g, could be expected in the other major city close to the Straits, Reggio Calabria. Average expected PGA values are in the range 0.3–0.6g. Recent findings of Zonno *et al.* (2008) corroborate this hypothesis.

In addition, we simulate ground shaking for the 1908 M_w 7.1 earthquake, using a slightly modified version of the Amoruso *et al.* (2006) slip model (Fig. 2). In this case, we find that the maximum possible experienced peak levels for Messina and Reggio Calabria were up to 0.6–0.7g for both cities. Interestingly, these values are lower than those obtained for a smaller earthquake of magnitude M_w 7.0 for the city of Messina. This can be reasonably traced back to the patchy character of the slip model and the relative station-slip patch positions. As shown by Cultrera *et al.* (2010), the relative position between nucleation point and slip patches with respect to the observation sites can strongly influence ground-shaking levels. This phenomenon of on-fault directivity, reported also by Mena & Mai (2011), thus plays an integral part in near-field ground-motion simulations. Moreover, we note that the maximum slip-rates on the fault are slightly larger for the M_w 7.0 earthquakes (that occur on a 40 by 20 km^2 fault plane) than for the M_w 7.1 rupture (on a 60 by 30 km^2 plane), thus reducing the peak ground-motions for the M_w 7.1 scenario. However, it should be underlined that, for both M_w 7.0 and 1908 M_w 7.1 events, our simulations do not consider basin effects or 3-D wave propagation effects that strongly modulate the resulting ground-shaking levels and their distribution (Graves *et al.* 1998; Benites & Olsen 2005; Imperatori *et al.* 2010). Although selecting a hypocentre position in southernmost part of the fault, in agreement with other authors (Michelini *et al.* 2005), the qualitative comparison between our synthetic PGA distribution and observed isoseismal maps for the 1908 event (Bottari *et al.* 1986) suggests that the Amoruso fault geometry fails to fully explain the mapped intensity pattern. Beside basin and 3-D wave-guide propagation effects, and the uncertainty affecting the damage mapping, we hypothesize that complex faulting on several fault segments need to be considered to reconcile the simulation results with the various data sets.

REFERENCES

Aagaard, B. T. *et al.*, 2008. Ground-motion modeling of the 1906 San Francisco earthquake, part ii: ground-motion estimates for the 1906 earthquake and scenario events, *Bull. seism. Soc. Am.,* **98**(2), 1012–1046.

Allen, T. & Wald, D., 2007. Topographic-slope as a proxy for seismic site-conditions (vs 30) and amplification around the globe, *US Geological Survey Open-File Report*.

Amoruso, A., Crescentini, L. & Scarpa, R., 2002. Source parameters of the 1908 Messina Straits, Italy, earthquake from geodetic and seismic data, *J. Geophys. Res.-Sol. Earth,* **107**(B4), 2080, doi:10.1029/2001JB000434.

Amoruso, A., Crescentini, L., Neri, G., Orecchio, B. & Scarpa, R., 2006. Spatial relation between the 1908 Messina Straits earthquake slip and recent earthquake distribution, *Geophys. Res. Lett.,* **33**(17), L17309, doi:10.1029/2006GL027227.

Andrews, D., 1976. Rupture propagation with finite stress in antiplane strain, *J. geophys. Res.,* **81**(20), 3575–3582.

Barberi, G., Cosentino, M., Gervasi, A., Guerra, I., Neri, G. & Orecchio, B., 2004. Crustal seismic tomography in the Calabrian Arc region, south Italy, *Phys. Earth planet. Inter.,* **147**(4), 297–314.

Basili, R., Valensise, G., Vannoli, P., Burrato, P., Fracassi, U., Mariano, S., Tiberti, M. & Boschi, E., 2008. The database of individual seismogenic sources (diss), version 3: summarizing 20 years of research on italy's earthquake geology, *Tectonophysics,* **453**(1–4), 20–43.

Benites, R. & Olsen, K., 2005. Modeling strong ground motion in the Wellington metropolitan area, New Zealand, *Bull. seism. Soc. Am.,* **95**(6), 2180–2196.

Billi, A., Funiciello, R., Minelli, L., Faccenna, C., Neri, G., Orecchio, B. & Presti, D., 2008. On the cause of the 1908 Messina tsunami, southern italy, *Geophys. Res. Lett.,* **35**(6), L06301, doi:10.1029/2008GL033251.

Boore, D., 1983. Stochastic simulation of high-frequency ground motions based on seismological models of the radiated spectra, *Bull. seism. Soc. Am.,* **73**(6), 1865–1894.

Boore, D. M. & Atkinson, G. M., 2008. Ground-motion prediction equations for the average horizontal component of PGA, PGV, and 5%-damped PSA at spectral periods between 0.01 s and 10.0 s, *Earthquake Spectra,* **24**(1), 99–138.

Borcherdt, R., 1994. Estimates of site-dependent response spectra for design (methodology and justification), *Earthq. Spectra,* **10,** 617–653.

Borcherdt, R., 2002. Empirical evidence for acceleration-dependent amplification factors, *Bull. seism. Soc. Am.,* **92**(2), 761–782.

Bottari, A., Carapezza, E., Carapezza, M., Carveni, P., Cefali, F., Giudice, E. L. & Pandolfo, C., 1986. The 1908 Messina Strait earthquake in the regional geostructural framework, *J. Geodyn.,* **5**(3–4), 275–302.

Bouchon, M., 1997. The state of stress on some faults of the san andreas system as inferred from near-field strong motion data, *J. Geophys. Res.-Sol. Earth,* **102**(B6), 11 731–11 744.

Brocher, T., 2005. Empirical relations between elastic wavespeeds and density in the Earth's crust, *Bull. seism. Soc. Am.,* **95**(6), 2081–2092.

Campbell, K.W. & Bozorgnia, Y., 2008. NGA ground motion model for the geometric mean horizontal component of PGA, PGV, PGD and 5% damped linear elastic response spectra for periods ranging from 0.01 to 10 s, *Earthq. Spectra,* **24**(1), 139–171.

Castro, R., Rovelli, A., Cocco, M., Bona, M. D. & Pacor, F., 2001. Stochastic simulation of strong-motion records from the 26 September 1997 (Mw 6), Umbria-Marche (Central Italy) earthquake, *Bull. seism. Soc. Am.,* **91**(1), 27–39.

Cultrera, G., Cirella, A., Spagnuolo, E., Herrero, A., Tinti, E. & Pacor, F., 2010. Variability of kinematic source parameters and its implication on the choice of the design scenario, *Bull. seism. Soc. Am.,* **100**(3), 941–953.

Day, S., 1982. 3-dimensional simulation of spontaneous rupture - the effect of nonuniform prestress, *Bull. seism. Soc. Am.,* **72**(6), 1881–1902.

Dunham, E., Favreau, P. & Carlson, J., 2003. A supershear transition mechanism for cracks, *Science,* **299**(5612), 1557–1559.

Graves, R. & Pitarka, A., 2004. Broadband ground motion simulation using a hybrid approach, *World Conference on Earthquake Engineering,* (Vancouver (BC), Canada, August 1–6, 2004).

Graves, R., Pitarka, A. & Somerville, P., 1998. Ground-motion amplification in the santa monica area: effects of shallow basin-edge structure, *Bull. seism. Soc. Am.,* **88**(5), 1224–1242.

Graves, R.W., Aagaard, B.T., Hudnut, K.W., Star, L.M., Stewart, J.P. & Jordan, T.H., 2008. Broadband simulations for Mw 7.8 southern San Andreas earthquakes: ground motion sensitivity to rupture speed, *Geophys. Res. Lett.,* **35**(22), L22302, doi:10.1029/2008GL035750.

Guatteri, M., Mai, P., Beroza, G. & Boatwright, J., 2003. Strong ground-motion prediction from stochastic-dynamic source models, *Bull. seism. Soc. Am.,* **93**(1), 301–313.

Guatteri, M., Mai, P. & Beroza, G., 2004. A pseudo dynamic approximation to dynamic rupture models for strong ground motion prediction, *Bull. seism. Soc. Am.,* **94**(6), 2051–2063.

Hartzell, S., Guatteri, M., Mai, P., Liu, P. & Fisk, M., 2005. Calculation of broadband time histories of ground motion, part ii: kinematic and dynamic modeling using theoretical Green's functions and comparison with the 1994 Northridge earthquake, *Bull. seism. Soc. Am.,* **95**(2), 614–645.

Hole, J., 1992. Nonlinear high-resolution 3-dimensional seismic travel time tomography, *J. Geophys. Res.-Sol. Earth,* **97**(B5), 6553–6562.

Imperatori, W., Aochi, H., Suhadolc, P., Douglas, J., Ducellier, A. & Costa, G., 2010. 2D versus 1D ground-motion modelling for the Friuli region, north-eastern Italy, *Bollettino di Geofisica Teorica ed Applicata,* **51**(1), 43–56.

Irikura, K., 1986. Prediction of strong acceleration motion using empirical Green's function, in *Proceedings of the 7th Japan Earthq. Eng. Symp,* pp. 151–156.

Kamae, K., Irikura, K. & Pitarka, A., 1998. A technique for simulating strong ground motion using hybrid Green's function, *Bull. seism. Soc. Am.,* **88**(2), 357–367.

Langer, H., Raffaele, R., Scaltrito, A. & Scarfi, L., 2007. Estimation of an optimum velocity model in the Calabro-Peloritan mountains-assessment of the variance of model parameters and variability of earthquake locations, *Geophys. J. Int.,* **170**(3), 1151–1164.

Liu, P., Archuleta, R. J. & Hartzell, S. H., 2006. Prediction of broadband ground-motion time histories: hybrid low/high-frequency method with correlated random source parameters, *Bull. seism. Soc. Am.,* **96**(6), 2118–2130.

Mai, P. & Beroza, G., 2002. A spatial random field model to characterize complexity in earthquake slip, *J. Geophys. Res.-Sol. Earth,* **107**(B11), 2308, doi:10.1029/2001JB000588.

Mai, P., Spudich, P. & Boatwright, J., 2005. Hypocenter locations in finite-source rupture models, *Bull. seism. Soc. Am.,* **95**(3), 965–980.

Mai, P.M., Imperatori, W. & Olsen, K.B., 2010. Hybrid broadband ground-motion simulations: combining long-period deterministic synthetics with high-frequency multiple S-to-S back-scattering, *Bull. seism. Soc. Am.,* **100**(5A), doi:10.1785/0120080194.

Mena, B. & Mai, P., 2011. Selection and quantification of near-fault velocity pulses owing to source directivity, *GEORISK,* **5**(1), 25–43.

Mena, B., Mai, P.M., Olsen, K.B., Purvance, M.D. & Brune, J.N., 2010. Hybrid broadband ground-motion simulation using scattering Green's functions: application to large-magnitude events, *Bull. seism. Soc. Am.,* **100**(5A), 2143–2162.

Michelini, A., Lomax, A., Nardi, A., Rossi, A., Palombo, B. & Bono, A., 2005. A modern re-examination of the locations of the 1905 Calabria and the 1908 Messina Straits earthquakes, *Geophys. Res. Abs.,* **7**(EGU05-A-07909).

Monaco, C. & Tortorici, L., 2000. Active faulting in the Calabrian arc and eastern Sicily, *J. Geodyn.,* **29**(3–5), 407–424.

Oglesby, D. & Day, S., 2002. Stochastic fault stress: implications for fault dynamics and ground motion, *Bull. seism. Soc. Am.,* **92**(8), 3006–3021.

Pino, N., Giardini, D. & Boschi, E., 2000. The December 28, 1908, Messina Straits, southern Italy, earthquake: waveform modeling of regional seismograms, *J. Geophys. Res.-Sol. Earth,* **105**(B11), 25 473–25 492.

Pino, N.A., Piatanesi, A., Valensise, G. & Boschi, E., 2009. The 28 December 1908 Messina Straits earthquake (Mw 7.1): a great earthquake throughout a century of seismology, *seism. Res. Lett.,* **80**(2), 243–259.

Pitarka, A., Somerville, P., Fukushima, Y., Uetake, T. & Irikura, K., 2000. Simulation of near-fault strong-ground motion using hybrid Green's functions, *Bull. seism. Soc. Am.,* **90**(3), 566–586.

Pulido, N. & Dalguer, L.A., 2009. Estimation of the high-frequency radiation of the 2000 Tottori (Japan) earthquake based on a dynamic model of fault rupture: application to the strong ground motion simulation, *Bull. seism. Soc. Am.,* **99**(4), 2305–2322.

Pulido, N. & Kubo, T., 2004. Near-fault strong motion complexity of the 2000 Tottori earthquake (Japan) from a broadband source asperity model, *Tectonophysics,* **390**(1–4), 177–192.

Ripperger, J. & Mai, P., 2004. Fast computation of static stress changes on 2D faults from final slip distributions, *Geophys. Res. Lett.,* **31**(18), L18610, doi:10.1029/2004GL020594.

Rosakis, A., Samudrala, O. & Coker, D., 1999. Cracks faster than the shear wave speed, *Science,* **284**(5418), 1337–1340.

Rosakis, A.J., Kanamori, H. & Xia, K., 2006. Laboratory earthquakes, *Int. J. Fracture,* **138**(1–4), 211–218.

Sato, H. & Fehler, M.C., 1994. *Seismic Wave Propagation and Scattering in the Heterogeneous Earth,* AIP Springer, New York.

Somerville, P., *et al.*, 1999. Characterizing crustal earthquake slip models for the prediction of strong ground motion, *Seism. Res. Lett.,* **70,** 59–80.

Spudich, P. & Xu, L., 2003. Software for calculating earthquake ground motions from finite faults in vertically varying media, *Int. Geophys.,* **81,** 1633–1634.

Star, L., Stewart, J., Graves, R. & Hudnut, K., 2008. Validation against NGA empirical model of simulated motions for M7.8 rupture of San Andreas fault, in *14th World Conference on Earthquake Engineering,* pp. 12–17.

Teramo, A., *et al.*, 2008. *Dal Terremoto Di Messina 1908 Alla Valutazione Di Scenari Di Danno Nel 2008-from the 1908 Messina Earthquake to Scenario Damage Assessment in 2008,* IUSS Press, ISBN 978-88-6198-027-3.

Tinti, E., Fukuyama, E., Piatanesi, A. & Cocco, M., 2005. A kinematic source-time function compatible with earthquake dynamics, *Bull. seism. Soc. Am.,* **95**(4), 1211–1223.

Tuvé, T., Bianco, F., Ibanez, J., Patane, D., Pezzo, E.D. & Bottari, A., 2006. Attenuation study in the Straits of Messina area (Southern Italy), *Tectonophysics,* **421**(3–4), 173–185.

Varela, C., Rosa, A. & Ulrych, T., 1993. Modeling of attenuation and dispersion, *Geophysics,* **58**(8), 1167–1173.

Wald, D., Quitoriano, V., Heaton, T. & Kanamori, H., 1999. Relationships between peak ground acceleration, peak ground velocity, and modified Mercalli intensity in California, *Earthq. Spectra,* **15**, 557.

Wells, D. & Coppersmith, K., 1994. New empirical relationships among magnitude, rupture length, rupture width, rupture area, and surface displacement, *Bull. seism. Soc. Am.,* **84**(4), 974–1002.

Zeng, Y., 1991. Compact solutions for multiple scattered wave energy in time domain, *Bull. seism. Soc. Am.,* **81**(3), 1022–1029.

Zeng, Y., 1993. Theory of scattered P-wave and S-wave energy in a random isotropic scattering medium, *Bull. seism. Soc. Am.,* **83**(4), 1264–1276.

Zeng, Y., Su, F. & Aki, K., 1991. Scattering wave energy propagation in a random isotropic scattering medium .1. theory, *J. Geophys. Res.-Sol. Earth,* **96**(B1), 607–619.

Zonno, G., Musacchio, G., Basili, R., Imperatori, W. & Mai, M. P., 2008. Stochastic and full-wavefield finite-fault ground-motion simulations of the Mw7.1, Messina 1908 earthquake (Southern Italy), Available at:*Earth-Prints*, *http://hdl.handle.net/2122/4742* (accessed in 2011 December 01).